Nanoscale Advances

ROYAL SOCIETY OF CHEMISTRY

PAPER

View Article Online
View Journal | View Issue

Open Access Article. Published on 31 March 2021. Downloaded on 4/29/2026 6:08:00 AM.
This article is licensed under a Creative Commons Attribution-NonCommercial 3.0 Unported Licence.

Check for updates

Cite this: *Nanoscale Adv.*, 2021, **3**, 2924

Heterogeneous assembly of Ni–Co layered double hydroxide/sulfonated graphene nanosheet composites as battery-type materials for hybrid supercapacitors†

Hua Tian,[a] Kaixin Zhu,[a] Yang Jiang,[a] Lin Wang,[*a] Wang Li,[a] Zhifeng Yu[a] and Cunqi Wu[*b]

Graphene-based hybrid composites as positive electrodes have aroused great interest in the field of hybrid supercapacitors. However, the charge storage capability of hybrid composites suffers from the scarce interaction between their end members to some extent. Herein, a hybrid composite with electrostatic interaction was obtained by employing a heterogeneous assembly strategy of Ni–Co layered double hydroxide (LDH) and sulfonated graphene nanosheets (SGN). Depending on the substitution of the negatively charged SGN for the interlayer nitrate anions compensating for the positively charged LDH host slabs, the abundance of Ni^{3+} on the surface of the hybrid composite could be increased to intensify the electrostatic interaction within hybrid composites. As expected, the effective coupling of LDH with SGN ensured the uniform incorporation of heterogeneous components. The unique structure of the hybrid composite accelerated electron transfer and ion diffusion processes during electrochemical reactions, which is beneficial to improve the electrochemical performance of battery-type electrodes. Further evaluation showed that the specific capacity of the LDH/SGN hybrid composite is 1177 C g^{-1} (2354 F g^{-1}) at 1 A g^{-1}. Additionally, the LDH/SGN//AC hybrid supercapacitor achieved an energy density of 43 W h kg^{-1} at 800 W kg^{-1} and still retained 94% of its initial specific capacitance over 10 000 cycles. The boosting effect of the electrostatic interaction within the hybrid composite on electrochemical properties offers a novel pathway for the development of supercapacitors.

Received 2nd January 2021
Accepted 30th March 2021

DOI: 10.1039/d1na00001b

rsc.li/nanoscale-advances

1 Introduction

Supercapacitors have attracted considerable attention over the last few decades in view of their fast charge–discharge capability and excellent cycling stability, which are deemed to be promising candidates for next-generation energy storage devices.[1–3] As is well known, the realization of advanced supercapacitors is strongly dependent on the electrical properties and ingenious structures of their constitutive materials.[4–7] However, despite the great progress achieved recently, energy storage systems with high power densities still suffer from low energy densities in comparison with rechargeable batteries. Among the significant approaches to resolve the above-mentioned limitation, the combination of multiple species is believed to make up for the low theoretical capacitances of electric double-layer capacitor materials (carbon nanotube, graphene and MXene) and the intrinsic carrier transport resistances of battery-type materials (transition metal hydroxides, transition metal oxides and transition metal sulfides) simultaneously to boost the whole energy and power densities for the demand of power supplies in electronic devices and electric vehicles.[8–13]

Consequently, numerous hybrid composites (metal–organic frameworks/carbon nanotubes, transition metal selenides/graphene and layered double hydroxides/MXenes) have been developed to promote the intrinsic nature of constitutive materials in terms of structural arrangement, electrical conductivity and mechanical stability.[14–22] Remarkably, it has been demonstrated that the existence of two-dimensional structures in hybrid composites can improve the effective contact between end members, facilitating the transport of electrons and ions during the electrochemical reaction.[23–25] For instance, Y. C. Jiang *et al.* proposed a facile *in situ* nucleation strategy to immobilize monodispersed Ni–Fe LDH ultrafine nanosheets on graphene oxide.[26] The composited Ni–Fe LDH@rGO electrode, which was regarded as a microreactor, could provide high specific capacitances and energy densities.

[a]*Hebei Key Laboratory of Applied Chemistry, College of Environmental and Chemical Engineering, Yanshan University, Qinhuangdao, 066004, China. E-mail: chinalinkwuang@126.com*

[b]*The State Key Laboratory of Electroanalytic, Changchun Institute of Applied Chemistry, Chinese Academy of Sciences, Changchun, 130022, China. E-mail: wucunqi@ciac.ac.cn*

† Electronic supplementary information (ESI) available. See DOI: 10.1039/d1na00001b

© 2021 The Author(s). Published by the Royal Society of Chemistry

Open Access Article. Published on 31 March 2021. Downloaded on 4/29/2026 6:08:00 AM.
This article is licensed under a Creative Commons Attribution-NonCommercial 3.0 Unported Licence.

Accordingly, there have been attempts to couple layered double hydroxide comprised of positively charged host layers and counter interlayer anions with graphene nanosheets through various methods such as hydrothermal treatment, *in situ* growth route and dip-coating process.[27–29] In particular, layered double hydroxides can be delaminated to positively charged inorganic macromolecules towards the exploitation of heterogeneous assembly methodologies due to the diversity of hierarchical structures in graphene-based hybrid composites.[30]

Besides, the emergence of integral microstructures in hybrid composites is a feasible route to enhance the electrochemical performance, and well-coupled structures are still pursued to mediate the surface electronic structures of electroactive species with the aim of increasing the number of electrochemical active sites and promoting the charge transport kinetics. Moreover, the establishment of chemical bonding within hybrid composites is beneficial to realize interfacial charge transfer, which in turn is advantageous due to the possible synergistic effect on charge storage capabilities. Herein, hybrid composites with electrostatic interaction were fabricated *via* a heterogeneous assembly strategy of Ni–Co layered double hydroxide and sulfonated graphene nanosheets. To construct the effective electrostatic interaction between the end members within the hybrid composites, nitrate anionic Ni–Co layered double hydroxide nanoclusters (LDH–NO_3) as positive constituents were prepared *via* an oxidation-induced anion intercalation process. Besides, two-dimensional graphene nanosheets with a sulfonated glucose structure as negative constituents were synthesized through the nitrogen doping of graphene oxide with glucosamine followed by sulfonating treatment in the presence of chlorosulfonic acid. During the heterogeneous assembly process, the substitution of the surface sulfonic groups anchored to the graphene nanosheets for interlayer nitrate anions in LDH–NO_3 gave rise to electrostatic connection between the LDH host layers and sulfonated graphene nanosheets. The appearance of the electrostatic interaction within hybrid composites is beneficial for the uniform distribution of LDH nanoclusters on the surface of the sulfonated graphene nanosheets together with an enhancement in the abundance of Ni^{3+} on the surface of the hybrid composites. Additionally, the reinforcement interaction within the LDH/SGN hybrid composites can expedite the electron transfer and ion diffusion processes during electrochemical reactions, and hence enhance the contribution of the diffusion-controlled processes to the charge storage processes, leading to an improvement in rate capacities and cycling stability for supercapacitors.

2 Experimental

2.1 Materials

Graphite powder with a lateral size in the range of 2 to 3 μm was used to obtain graphite oxide (GO) according to a modified Hummers method.[31–33] Glucosamine sulfate, chlorosulfonic acid, cobalt nitrate hexahydrate, nickel nitrate hexahydrate and ammonium carbonate of analytical purity were purchased from Aladdin Corporation, China. Activated carbon (AC) was obtained from Kuraray Trading Co., Ltd.

2.2 Synthesis of glucosamine-modified graphene nanosheets

Glucosamine-modified graphene nanosheets (GGN) were synthesized from as-prepared GO *via* a nitrogen doping procedure. Typically, 1.2 g of glucosamine sulfate was dissolved in 50 mL of 0.8 mg mL^{-1} GO aqueous solution with stirring for 30 min. Sequentially, 0.2 g of sodium hydroxide was added into the above solution and heated at 80 °C with continuous stirring for 8 h. The residue was then collected by centrifugation after washing with deionized water several times, followed by a vacuum freeze-drying process for further characterization. Afterwards, 0.02 g of the resulting powder was dispersed in 200 mL of deionized water under ultrasonication to obtain a stable colloidal dispersion, and then centrifuged at 1000 rpm for 10 min to remove larger aggregates for the fabrication of hybrid composites.

2.3 Synthesis of sulfonated graphene nanosheets

Sulfonated graphene nanosheets were synthesized through sulfonating treatment of the as-prepared GGN powder in the presence of chlorosulfonic acid. Typically, 0.1 g of as-prepared GGN powder was dispersed in 40 mL of dichloromethane with vigorous stirring. Then, 2 mL of chlorosulfonate acid was added dropwise into the above suspension and stirred continuously at room temperature overnight. The deposit was washed with deionized water by repeated centrifugation until the supernatant was neutral, and then vacuum freeze-dried for further characterization. Finally, 0.02 g of the resulting powder was dispersed in 200 mL of deionized water and subjected to ultrasonication to form a homogeneous colloidal dispersion, followed by centrifugation at 1000 rpm for 10 min to remove larger aggregates for the fabrication of hybrid composites.

2.4 Synthesis of LDH–NO_3 nanoclusters

LDH–NO_3 nanoclusters were obtained using an oxidation-induced anion intercalation strategy. Typically, 0.15 g of ammonium carbonate was added to 30 mL of absolute ethanol and heated at 50 °C with moderate stirring. After dissolving completely, 0.4 g of nickel nitrate hexahydrate and 0.8 g of cobalt nitrate hexahydrate were added to the above solution and stirred at 50 °C for 2 h. Subsequently, 50 mL of 0.8 wt% hydrogen peroxide aqueous solution containing 6.5 g of sodium nitrate was mixed with the above mixture *via* continuous stirring for additional 3 h. The deposit was washed with deionized water several times by centrifugation, and then vacuum freeze-dried for further characterization. Finally, 0.2 g of the resulting powder was dispersed in 400 mL of deionized water under ultrasonication to form a homogeneous colloidal dispersion, and then centrifuged at 1000 rpm for 10 min to remove larger aggregates for the fabrication of hybrid composites.

Open Access Article. Published on 31 March 2021. Downloaded on 4/29/2026 6:08:00 AM.
This article is licensed under a Creative Commons Attribution-NonCommercial 3.0 Unported Licence.

2.5 Fabrication of LDH/SGN hybrid composites

The fabrication of LDH/SGN hybrid composites was realized by virtue of a heterogeneous assembly process of as-prepared LDH and SGN. Typically, 200 mL of as-prepared SGN dispersion was added to 400 mL of as-prepared LDH–NO_3 dispersion and stirred mechanically at room temperature overnight. After standing for a while, the resulting deposit was collected by filtration and washed with deionized water several times prior to a freeze-drying process. For comparison, LDH/GGN hybrid composites were also prepared under similar conditions with GGN instead of SGN dispersion.

2.6 Material characterization

Powder X-ray diffraction (XRD) analysis was performed using a Rigaku D/MAX-RC X-ray diffractometer to identify the crystalline phases of the as-prepared samples. The morphologies of the as-prepared samples were observed on a transmission electron microscope (TEM, JEOL, JEM-2100, 200 kV) and field emission scanning electron microscope (FESEM, Hitachi, S-4800, 15 kV). Fourier transform infrared (FT-IR) spectra were recorded on a PerkinElmer Spectrum One spectrophotometer using KBr disks in the range of 500 to 4000 cm^{-1}. X-ray photoelectron spectroscopy (XPS) measurements were carried out on a Kratos Axis Ultra-DLD spectrometer equipped with monochromatic Al–K radiation ($h\nu$ = 1486.6 eV). The carbonaceous C 1s line (284.6 eV) served as the reference to calibrate the binding energies (BEs). Thermogravimetric (TG) analysis was performed using a PerkinElmer Pyris 1 TGA thermo balance. In the TG experiment, the as-prepared samples were heated from 30 °C to 700 °C at 10 °C min^{-1} in an air atmosphere. The zeta potential of the as-prepared dispersions was investigated using a Brookhaven 90 Plus PALS analyzer.

2.7 Electrochemical measurements

The individual electrodes used in the electrochemical measurements were fabricated by mixing 85 wt% as-prepared powder with 5 wt% acetylene black and 10 wt% polytetrafluorene ethylene (PTFE) binder. A small amount of deionized water was added to the above mixture to obtain a homogeneous paste. The as-obtained paste was then pressed onto nickel foam current collectors (1.0 cm × 1.0 cm) and dried at 60 °C for 12 h. Moreover, each electrode contained around 2 mg cm^{-2} of electroactive materials. The electrochemical tests of the as-prepared electrodes were performed using a conventional three-electrode cell, in which platinum foil and Hg/HgO electrodes were applied as the counter and reference electrodes, respectively. In addition, the hybrid supercapacitor (LDH/SGN//AC) was assembled using LDH/SGN hybrid composites as positive electrodes and activated carbon (AC) as negative electrodes with porous non-woven cloths as separators, according to our previous report.[34] The loading mass ratio of active materials between the positive and negative electrodes was 0.35. All electrochemical measurements were carried out in 6 M KOH aqueous solution at room temperature. Cyclic voltammetry (CV) and electrochemical impedance spectroscopy (EIS) measurements were conducted on a CHI 604E electrochemical workstation (Shanghai CH Instrument Company, China). Galvanostatic charge–discharge (GCD) and voltage holding tests were investigated using a Neware battery testing workstation.

3 Results and discussion

The distribution of the hybrid composites with electrostatic interaction based on the heterogeneous assembly process between LDH–NO_3 and SGN is illustrated in Fig. 1. The emergence of the LDH/SGN hybrid composite depends mainly on the anionic modification of LDH as the positive constituent and surface functionalization of graphene nanosheets as the negative constituents. To build positively charged LDH host layers, transition metal complexes were firstly obtained *via* the decomposition of ammonium carbonate under anhydrous conditions. In the subsequent hydrolysis process, hydrogen peroxide served as an oxidant to partially transform the transition metals from the divalent to trivalent state, which is beneficial to attract oppositely charged counterparts for the formation of nanocluster architectures. Also, to promote the anion-exchange capability of LDH, nitrate anions were intercalated in the interlamellar region towards charge balancing in the lamellar structure under the assistance of an aqueous solution of sodium nitrate. Furthermore, the graphene nanosheets were endowed with electrical conductivity and surface electronegativity *via* a nitrogen doping process followed by sulfonating treatment. The nitrogen doping of graphite oxide with glucosamine resulted in the formation of continuous conjugated structures to allow lateral electron migration, together with the immobilization of redundant hydroxyl groups to two-dimension carbonaceous scaffolds. Importantly, the massive hydroxyl groups on the surface of GGN could integrate covalently with sulfonic groups to ensure available dispersibility and enriched negative bridging sites. As expected, the mixing of the positively charged LDH–NO_3 with negatively charged SGN induced the substitution of sulfonic groups anchored to SGN for interlayer nitrate anions located in LDH through the anion-

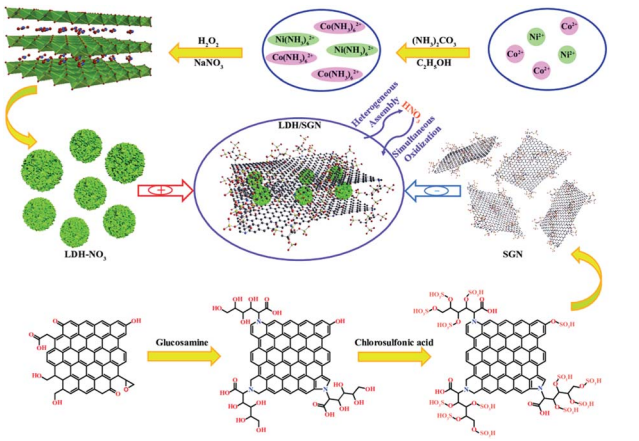

Fig. 1 Schematic illustration of the heterogeneous assembly strategy of LDH/SGN.

 © 2021 The Author(s). Published by the Royal Society of Chemistry

Open Access Article. Published on 31 March 2021. Downloaded on 4/29/2026 6:08:00 AM.
This article is licensed under a Creative Commons Attribution-NonCommercial 3.0 Unported Licence.

exchange reaction together with the generation of nitric acid molecules, aiming to establish electrostatic connection between the end members. Notably, the appearance of nitric acid molecules could re-oxidize the transition metals, leading to an excess of trivalent metal ions in the LDH host layers, which was conducive to consolidating the electrostatic interaction within the hybrid composites.

Zeta potential analysis (Fig. 2a) was used to evaluate the charge states of the as-prepared dispersions. Notably, the zeta potential of the LDH–NO_3 dispersion at 24.8 mV indicates the positively charged surface of the LDH host layers, approaching the critical potential line at 25 mV to maintain the indispensable stability of dispersion system.[35,36] In this case, the suitable magnitude of the electrostatic repulsion between individual LDH–NO_3 nanoclusters is capable of stabilizing the corresponding dispersions for over 48 h. Additionally, both the GGN and SGN dispersions exhibited negative zeta potentials, proving that the introduction of hydroxyl and sulfonic groups to the carbon panels is favorable to generate negative surface charges. The low zeta potential of the SGN dispersion at −26.7 mV relative to that of the GGN dispersion at −16.4 mV is attributed to the high ionization efficiency of the sulfonic groups, which tends to quantitatively increase the negative bridging sites, strengthening the electrostatic attraction to the positively charged inorganic macromolecules. Remarkably, the mixing of LDH–NO_3 with graphene-based dispersions realized the heterogeneous assembly process based on the mutual attraction between the heterogeneous constituents, thus separating the black flocculants.

The crystal features of the as-prepared samples were explored by X-ray diffraction analysis. As depicted in Fig. S1,† the broad diffraction peak of GGN at around 24.3° can be well indexed to the (002) plane of graphene nanosheets with the *d*-spacing distance of 0.36 nm, where the nitrogen doping of GO with glucosamine leads to the disordered stacking structure of carbonaceous nanosheets accompanied by the effective removal of the oxygen-containing functional groups. By comparison, the similar XRD pattern of SGN indicates the desirable stability of the graphene scaffolds during the successive sulfonating process. Fig. 2b shows the characteristic diffraction peaks of LDH–NO_3 at 11.58°, 22.48°, 35.04° and 61.04°, corresponding to the (003), (006), (012) and (110) planes of the hydrotalcite-like Ni–Co carbonate hydroxide hydrate phase (JCPDS no. 40-0216), respectively. The above result demonstrates the successful formation of LDH upon applying the oxidation-induced anion intercalation strategy. Moreover, both hybrid composites also exhibit the typical XRD pattern of LDH, illustrating the smooth integration of negatively charged graphene nanosheets and positively charged LDH nanoclusters under the electrostatic attraction between them. However, it is difficult to observe the characteristic diffraction peaks of graphene-based carbon materials, proving the complete exfoliation state of graphene nanosheets after the heterogeneous assembly process.

To explain the formation mechanism of hybrid composites with electrostatic interaction, Fourier transform infrared spectroscopy was used to inspect the chemical compositions of the as-prepared samples. Prior to the heterogeneous assembly process, the FT-IR spectra of the graphene-based carbon materials are presented in Fig. S2.† The characteristic peaks of GGN at 1640, 1394 and 1207 cm^{-1} correspond to the C=C, C–OH and C–N stretching vibrations, respectively.[37–39] This confirms the immobilization of hydroxyl groups on the surface of the graphene scaffolds with the aid of the nitrogen doping of GO with glucosamine, which is consistent with the results from the XPS spectra in Fig. S3.† Remarkably, the two additional peaks for SGN at 1125 and 1055 cm^{-1} can be ascribed to the symmetric and asymmetric O=S=O stretching vibrations, respectively, suggesting the junction of the sulfonic groups with hydroxyl groups in covalent bonds.[40,41] Upon mixing the graphene-based carbon materials with LDH–NO_3, Fig. 2c depicts the FT-IR spectra of the LDH–NO_3 and hybrid composites. The broad band at 3435 cm^{-1} is associated with the O–H stretching vibrations of the hydroxyl groups in the LDH host layers and intercalated H_2O molecules. The appearance of the characteristic band at 1630 cm^{-1} is attributed to the bending vibrations of the intercalated H_2O molecules.[42] In addition, the sharp bond of LDH–NO_3 at 1384 cm^{-1} is assigned to the stretching vibrations of NO_3^-, indicating the predictable intercalation of NO_3^- anions in the interlamellar region of LDH.[43] Remarkably, the attenuation of the corresponding bands for the hybrid composites indicates that the integration of the heterogeneous constituents arises from the employment of negatively charged groups anchored to the surface of the graphene framework instead of the interlayer NO_3^- anions located in LDH–NO_3.

Thermogravimetric analyses were carried out in an air atmosphere to clarify the substance compositions of the hybrid composites. As shown in Fig. 2d, the initial mass loss of the as-prepared samples below 200 °C results from the evaporation of physically and chemically adsorbed water. The major mass loss of LDH–NO_3 in the temperature range of 200 °C to 300 °C is ascribed to the dehydroxylation of the brucite-like layers,

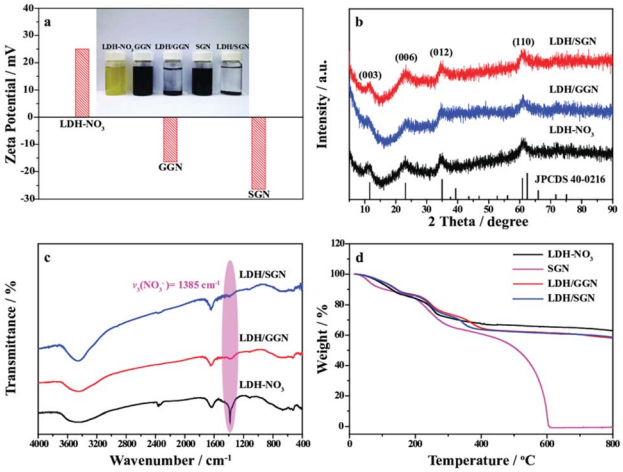

Fig. 2 Structural characterization of as-prepared samples. (a) Zeta potential distribution of as-prepared dispersions with corresponding digital photographs in the inset. (b) XRD patterns. (c) FT-IR spectra. (d) TG curves.

Open Access Article. Published on 31 March 2021. Downloaded on 4/29/2026 6:08:00 AM.
This article is licensed under a Creative Commons Attribution-NonCommercial 3.0 Unported Licence.

followed by an inconspicuous mass loss above 300 °C owing to the decomposition of the interlayer anions.[44,45] Moreover, the mass loss of SGN also undergoes two additional domains including the removal of functional groups from 200 °C to 400 °C and combustion of carbonaceous scaffolds above 400 °C. In this context, the mass loss of LDH–NO_3 and SGN was determined to be 37.2% and 99.6% with an increase in temperature to 800 °C, respectively. Interestingly, the LDH/GGN and LDH/SGN hybrid composites exhibited an obvious combination of thermal decomposition behaviors between LDH–NO_3 and graphene together with a total mass loss of 41.9% and 41.4% at 800 °C. Therefore, the contents of the graphene-based carbon materials within hybrid composites can be calculated to be 7.5% and 6.7%, respectively. The similarity of the substance components between the LDH/GGN and LDH/SGN hybrid composites suggests that the significant advantage of charge storage capabilities benefits principally from the enhanced electrostatic attraction between the end members.

Furthermore, the microstructures were investigated *via* scanning electron microscopy and transmission electron microscopy. Fig. S4† shows that the nanocluster-like architecture of LDH–NO_3 with a size of around 150 nm consists of interconnected flake-like nanopetals. The observation for SGN (Fig. S5†) indicates partially wrinkled nanosheets with curly edges. Moreover, the detailed information on the morphologies of the LDH/SGN hybrid composites is presented in Fig. 3. The SEM image (Fig. 3a) reveals the uniform incorporation of intact LDH nanoclusters in the uneven surface of SGN in comparison with the loose crumb structure of the LDH/GGN hybrid composite (Fig. S5†), accompanied by the corresponding elemental mapping with the homogeneous distribution of elemental Ni, Co, O, N, S and C. This result suggests that the emergence of the electrostatic interaction facilitates the well-organized integration of the SGN nanosheets with the LDH nanoclusters, which is favorable to allow the sufficient exposure of surface active sites in electrodes to the electrolyte. With respect to the TEM image in Fig. 3b, it is interesting to note the intimate interfacial adhesion of the LDH nanoclusters on the elastic surface of the SGN nanosheets after the ultrasonic treatment, illustrating the significance of the electrostatic interaction to maintain the structural integrity of the hybrid composites. Obviously, Fig. 3c depicts well-defined lattice fringes with *d*-spacings of 0.262 and 0.152 nm, corresponding well to the (012) and (110) planes of Ni–Co layered double hydroxide, respectively. The selected area electron diffraction (SAED) pattern of the LDH/SGN hybrid composite (Fig. 3d) shows a set of diffraction rings in relation to the polycrystalline nature of LDH, which is in good agreement with the above results from the XRD patterns.

For further examination of the surface chemical states of the electrode materials, X-ray photoelectron spectroscopy was employed to identify the chemical valence states of their elemental compositions, as shown in Fig. 4. The high-resolution Ni 2p XPS spectra (Fig. 4a) can be well split to two spin-orbit doublets together with two shake-up satellites. The appearance of doublets at binding energies of 855.3 and 872.9 eV corresponds to the oxidation state of Ni^{2+} in association with the other doublets at binding energies of 856.3 and 873.9 eV, which are the characteristic peaks of Ni^{3+}.[46] Interestingly, Fig. 4b shows that the presence of SGN is capable of enhancing the abundance of Ni^{3+} on the surface of the hybrid composite relative to GGN. This distinction of surface chemical states is attributed to the existence of strongly acidic groups anchored to the graphene framework, which contribute to the increase in the number of nitric acid molecules during the heterogeneous assembly process, promoting the tendency of nickel elements to high valence states. Importantly, the conductive graphene panels can accelerate the charge storage reactions of the active substances depending on the enhancement of trivalent nickel ions in the electrostatic interaction between SGN and LDH. Besides, the deconvolution of the high-resolution Co 2p XPS spectra (Fig. 4c) is dominated by spin-orbit doublets of Co^{2+} at binding energies of 782.4 and 797.9 eV

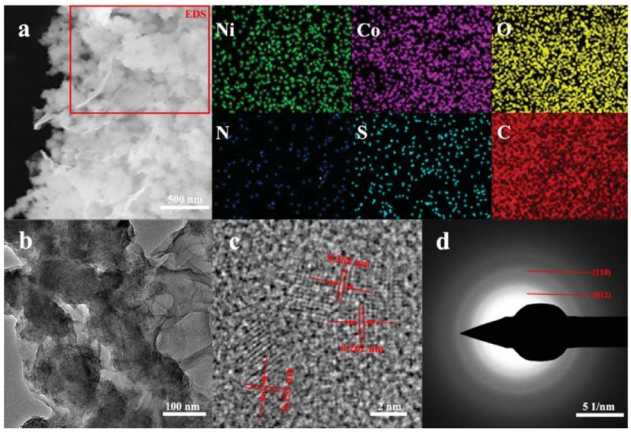

Fig. 3 Morphological characterizations of LDH/SGN. (a) SEM image with corresponding EDS mapping of Ni, Co, O, N, S and C elements. (b) TEM image. (c) HRTEM image. (d) SAED pattern.

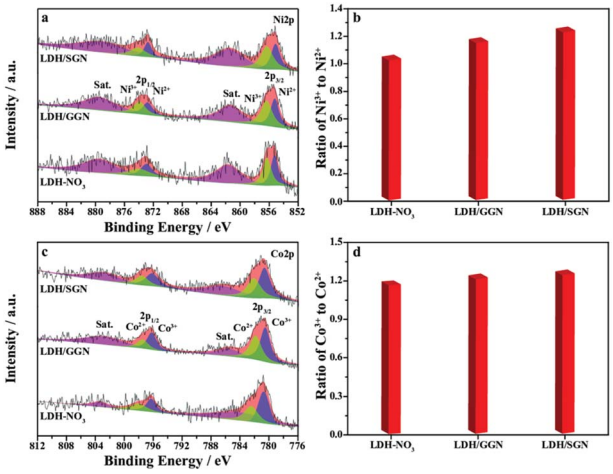

Fig. 4 XPS measurements of electrode materials. (a) Ni 2p XPS spectra. (b) Comparison of the ratio distribution between Ni^{3+} and Ni^{2+}. (c) Co 2p XPS spectra. (d) Comparison of the ratio distribution between Co^{3+} and Co^{2+}.

 © 2021 The Author(s). Published by the Royal Society of Chemistry

Open Access Article. Published on 31 March 2021. Downloaded on 4/29/2026 6:08:00 AM.
This article is licensed under a Creative Commons Attribution-NonCommercial 3.0 Unported Licence.

together with that of Co^{3+} at binding energies of 780.7 and 796.3 eV.[47] However, the slight variation in the ratio of Co^{3+} to Co^{2+} among all the electrode materials (Fig. 4d) implies the stabilization effect of cobalt elements as building blocks on the LDH host layers in addition to the predominance of nickel elements to increase the transport channels of the interfacial charge carriers.

To evaluate the significance of the electrostatic interaction in the hybrid composites on the advancement of charge storage capabilities, cyclic voltammetry and galvanostatic charge–discharge measurements were conducted in a three-electrode cell. The CV curves of the LDH–NO_3 and hybrid composites at a scan rate of 5 mV s^{-1} are shown in Fig. 5a. By comparison with the rectangle loop of graphene-based carbon materials (Fig. S6†), a pair of redox peaks at potentials of 0.41 and 0.08 V can be observed, which is associated with the reversible transition between the divalent and trivalent states of elemental nickel and cobalt, respectively. The possible electrochemical reactions are described as follows:[48–51]

$$Ni(OH)_2 + OH^- \underset{\text{discharge}}{\overset{\text{charge}}{\rightleftharpoons}} NiOOH + H_2O$$

$$Co(OH)_2 + OH^- \underset{\text{discharge}}{\overset{\text{charge}}{\rightleftharpoons}} CoOOH + H_2O$$

$$CoOOH + OH^- \underset{\text{discharge}}{\overset{\text{charge}}{\rightleftharpoons}} CoO_2 + H_2O$$

Importantly, the remarkable expansion of capacitive loops for the LDH/SGN hybrid composite implies the promotion of negatively charged groups anchored to the surface of the graphene framework with the utilization of the active compositions

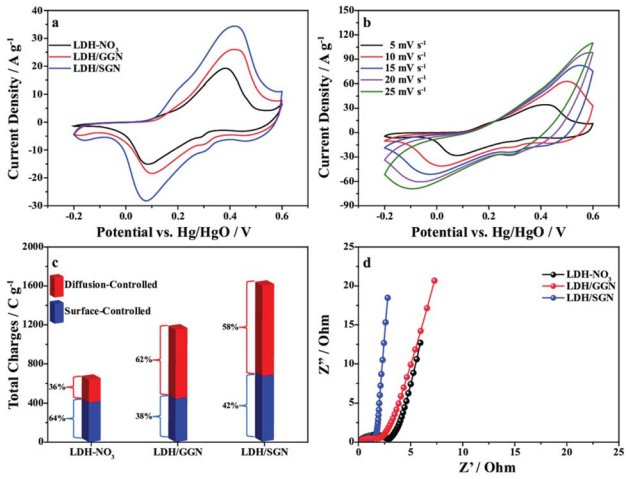

Fig. 5 Electrochemical characterization of electrode materials. (a) CV curves at 5 mV s^{-1}. (b) CV curves of LDH/SGN at various scan rates. (c) Comparison of charge storage contributions from the surface-controlled and diffusion-controlled reactions. (d) Nyquist plots with an AC voltage amplitude of 5 mV in the frequency range of 0.1–100 kHz at open circuit potential.

within LDH during the charge storage processes. Fig. 5b shows that the cathodic and anodic peaks of the LDH/SGN hybrid composites shift towards the negative and positive potential directions with similar shapes upon an increase in the scan rate, respectively, illustrating the unique faradic redox behavior to satisfy the demand for fast charge–discharge processes. Furthermore, the kinetic characteristics of the above electrochemical reactions can be evaluated using the relationship between peak current (i) and scan rate (v) as $i = av^b$, in which the value of b as a critical metric provides further insight into the charge storage mechanism.[52] As shown in Fig. S7,† the value of b can be obtained from the slope of the double logarithmic curve between peak current and scan rate. The values of b calculated for LDH–NO_3, LDH/GNN and LDH/SGN hybrid composites approach 0.5, indicating that all the electrode materials belong to battery-type electrodes with diffusion-controlled predominant processes. Notably, the steepest slope of the fitting curves for the LDH/SGN hybrid composite among the electrode materials suggests that the intensive electrostatic interaction within hybrid composites contributes to establishing effective transport channels for the active protons, accelerating the diffusion processes during electrochemical reactions.

In addition, the Trasatti method was performed to differentiate the charge storage contributions from the surface-controlled and diffusion-controlled reactions. The total charge (q_T) of the electrode materials was separated into two parts, *i.e.*, surface-controlled (q_s) and diffusion-controlled charges (q_d) as follows:[53]

$$q_T = q_s + q_d$$

Fig. 5c clearly shows that the presence of GGN within the hybrid composites increases merely the diffusion-controlled charge in comparison with LDH–NO_3, and hence moderately enhances the total charge together with the elevation of the contribution of diffusion-controlled reactions. Interestingly, the surface-controlled and diffusion-controlled charges of the LDH/SGN hybrid composites were both boosted together to maximize the total charge of the electrode materials, which is beneficial due to the fact that the electrostatic connection between SGN and LDH not only increases the number of active sites participating in the charge storage reactions but also affords abundant transfer pathways of active protons in the bulk phase of LDH. For further understanding the kinetic behavior, the Nyquist plots of the electrode materials from the electrochemical impedance spectroscopy measurements are presented in Fig. 5d. The intersection with x-axis in the high-frequency region represents the equivalent series resistance (R_s), and the diameter of the semicircles represents the charge transfer resistance (R_{CT}). Remarkably, all the electrode materials exhibit a similar juncture on the x-axis, indicating the nearly identical electrical conductivity. Besides, it can be seen that the LDH/SGN hybrid composite exhibits the smallest semicircle diameter among the electrode materials, corresponding to its lowest charge-transfer resistance. This suggests that the electrostatic interaction within the LDH/SGN hybrid composite speeds up

Open Access Article. Published on 31 March 2021. Downloaded on 4/29/2026 6:08:00 AM.
This article is licensed under a Creative Commons Attribution-NonCommercial 3.0 Unported Licence.

the electrochemical reactions of transition metal species on the surface of LDH, facilitating the charge transfer processes at the electrode/electrolyte interface to improve the power capabilities of energy storage devices.

Fig. 6a shows the galvanostatic charge–discharge curves of the electrode materials at a current density of 1 A g^{-1}, in which the distinct potential plateaus are directly related to the faradic characteristics of the battery-type electrodes. Additionally, the symmetrical characteristic of the GCD curves indicates the outstanding electrochemical reversibility of the electrode materials with high coulombic efficiency, which is in good agreement with the results from the CV curves. The discharge time of the LDH/SGN hybrid composite is notably prolonged in comparison with the other electrode materials, suggesting its superior charge storage capability among the electrode materials. As shown in Fig. 6b, the GCD curves of the LDH/SGN hybrid composite exhibit a similar shape with a rapid increase in current density, demonstrating that the electrostatic connection within the hybrid composites is beneficial for fast electrochemical reactions. Moreover, the specific capacities (C_s) were calculated from the corresponding GCD curves (Fig. S8†) using the following equation:[54]

$$C_s = \frac{i \times t}{m}$$

where i, t, and m represent the current density, discharge time and mass of active substances, respectively. Fig. 6c shows that the specific capacities of the LDH–NO_3, LDH/GGN and LDH/SGN hybrid composites were calculated to be 802, 1056 and 1177 C g^{-1} (1604, 2112 and 2354 F g^{-1}) at a current density of 1 A g^{-1}, respectively. With an increase in the current density to 10 A g^{-1}, the specific capacity decreased to 696, 742 and 880 C g^{-1} (1392, 1484 and 1760 F g^{-1}), respectively, illustrating that the electrostatic interaction within hybrid composites contributes to the conservation of charge storage capabilities under the operating condition of extreme current densities. Due to the fact that the cycling life of electrode materials is an important requirement for practical applications, a cycling test was carried out at a current density of 5 A g^{-1}, as shown in Fig. 6d. After 4000 cycles, the LDH–NO_3, LDH/GGN and LDH/SGN hybrid composites still retained 84%, 75% and 89% of their initial specific capacities, respectively. The improvement in the cycling stability of the LDH/SGN hybrid composite depends mainly on the suppression of the capacity loss on the sulfonated graphene nanosheets in the hybrid composite at the earlier stage of the cycling test, where the electrostatic interaction within the hybrid composite restrains the collapse of its microstructures and dissolution of its active substances.

To survey the practical applications of the LDH/SGN hybrid composite, a hybrid supercapacitor was also assembled using the LDH/SGN hybrid composite as the positive electrode and activated carbon as the negative electrode. Fig. 7a shows the CV curves of the LDH/SGN hybrid composite, activated carbon and pristine Ni foam at a scan rate of 5 mV s^{-1}. To balance the charge stored in both electrodes, the mass ratio of LDH/SGN hybrid composite to activated carbon was determined to be 0.35 based on the capacity values calculated from the above CV curves using the following equation:[55]

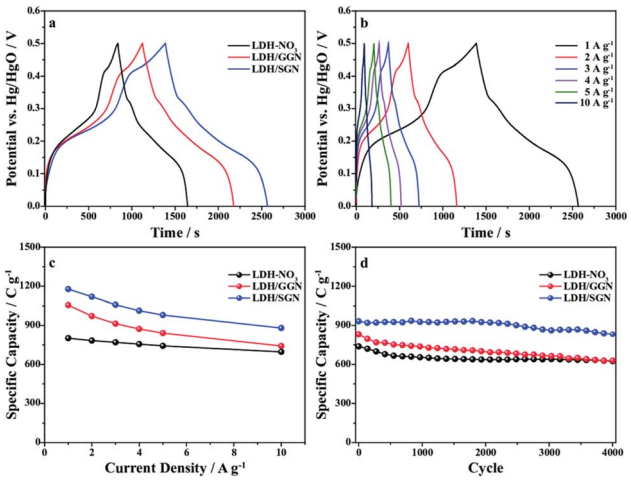

Fig. 6 GCD measurements of electrode materials. (a) GCD profiles at 1 A g^{-1}. (b) GCD profiles of LDH/SGN at various current densities. (c) Comparison of specific capacities at different current densities. (d) Cycling performance at 5 A g^{-1}.

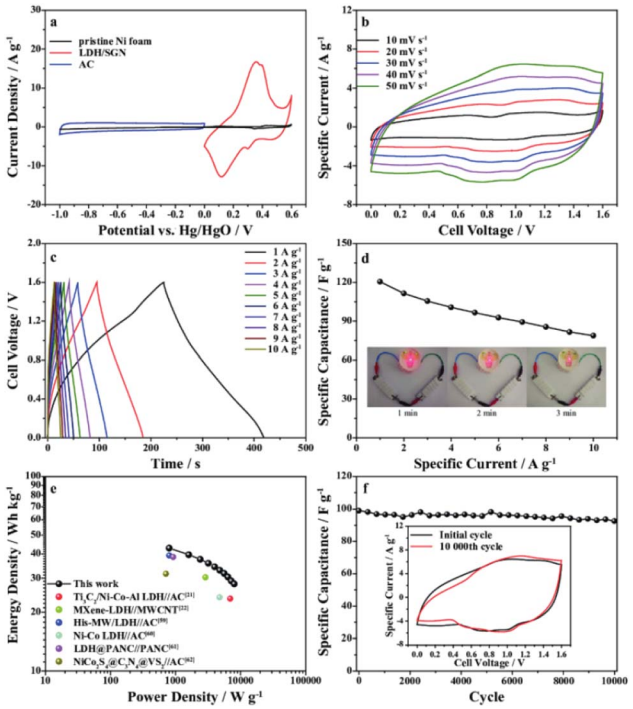

Fig. 7 Electrochemical performance of LDH/SGN//AC hybrid supercapacitor. (a) CV curves of LDH/SGN, AC and pristine Ni foam electrodes at 5 mV s^{-1}. (b) CV curves of the hybrid supercapacitor at various scan rates. (c) GCD profiles of the hybrid supercapacitor at different specific currents. (d) Normalized specific capacitances of the hybrid supercapacitor at different specific currents with digital photographs of three parallel LED indicators lit up by two series devices in the inset. (e) Ragone plots related to the energy and power densities. (f) Cycling performance at 2 A g^{-1} with CV curves at 50 mV s^{-1} before and after 10 000 cycles in the inset.

 © 2021 The Author(s). Published by the Royal Society of Chemistry

Open Access Article. Published on 31 March 2021. Downloaded on 4/29/2026 6:08:00 AM.
This article is licensed under a Creative Commons Attribution-NonCommercial 3.0 Unported Licence.

$$\frac{m_+}{m_-} = \frac{C_{s-}}{C_{s+}}$$

Moreover, the CV curve of the pristine Ni foam exhibited a small current density, implying the negligible capacitive contribution for the hybrid supercapacitor. The CV curves of the LDH/SGN//AC hybrid supercapacitor within different voltage windows ranging from 0.8 to 1.6 V were measured at a scan rate of 50 mV s^{-1} (Fig. S9a†). As observed, the hybrid supercapacitor exhibited a quasi-rectangular shape in the CV curves with redox peaks derived from faradic reactions after the voltage window exceeded 1.0 V. Meanwhile, the corresponding GCD curves (Fig. S9b†) indicate that the hybrid supercapacitor within a voltage window of 1.6 V delivers a maximum discharge time, signifying the optimum charge storage capability with the high coulomb efficiency in the absence of oxygen evolution caused by the decomposition of the electrolyte. In this case, the CV curves of the hybrid supercapacitor at various scan rates are shown in Fig. 7b. With an increase in the scan rate, it is evident that the hybrid supercapacitor could maintain a similar geometric pattern together with the obvious expansion of the capacitive loops, which is dependent on the combination between battery-type and capacitive behaviors.

Moreover, Fig. 7c shows the symmetrical quasi-triangle GCD profiles of the hybrid supercapacitor at various specific currents, proving the well-balanced charge storage in both electrodes. Based on the total mass of active materials in both electrodes, the specific capacitances (C_{sp}) of the hybrid supercapacitor were calculated from the GCD curves according to the following equation:[56,57]

$$C_{sp} = \frac{I \times \Delta t}{m \times \Delta V}$$

where I is the discharge current (A), Δt is the discharge time (s), m is the mass of active materials (g) and ΔV is the operating voltage (V). Fig. 7d shows that specific capacitances of the hybrid supercapacitor range from 121 to 80 F g^{-1} with an increase in specific current from 1 to 10 A g^{-1}. Interestingly, the digital photographs in the inset depict that two series-connected hybrid supercapacitors could efficiently light three commercial LED indicators (2.0 V, 20 mA) in parallel for 3 min, suggesting the commercial applications of the LDH/SGN hybrid composite for supercapacitors. Furthermore, the Ragone plot of the LDH/SGN//AC hybrid supercapacitor clarifies the relationship between the energy and power density, as shown in Fig. 7e. In accordance with the GCD curves of the hybrid supercapacitor, the energy (E) and power (P) densities were calculated using the following equations:[58]

$$E = \frac{C_{sp} \times V^2}{2}$$

$$P = E/\Delta t$$

where V is the discharge voltage range (V) and Δt is the discharge time (s). The hybrid supercapacitor delivered an energy density of 43 W h kg^{-1} at a power density of 800 W kg^{-1}. Even at a power density of 8000 W g^{-1}, the hybrid supercapacitor still retained an energy density of 28 W h kg^{-1}, which is superior to that of most of the recently reported devices based on Ni, Co, and other transition metal compounds.[21,22,59–62] As can be seen in Fig. 7f, the hybrid supercapacitor exhibited an excellence cycling performance with the capacitance retention of 94% in continuous operation for 10 000 cycles. Importantly, the inset (Fig. 7f) reveals the inconspicuous variation in the CV curves before and after the long-term cycling test, demonstrating the sufficient stability of the LDH/SGN hybrid composite as a positive electrode for hybrid supercapacitors.

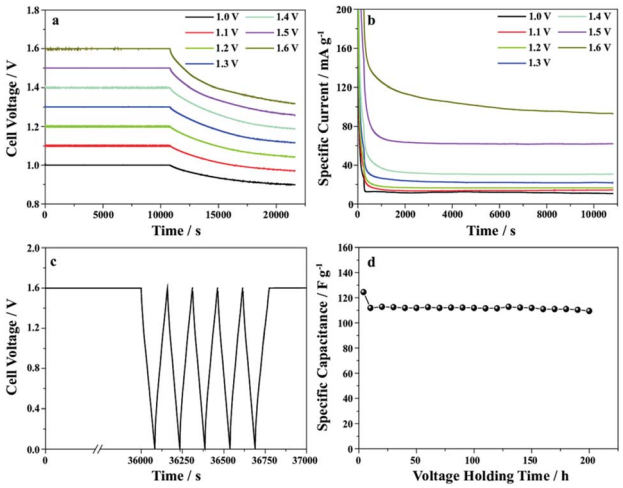

Fig. 8 Voltage holding test of LDH/SGN//AC hybrid supercapacitor. (a) Self-discharge tests after voltage holding tests for 3 h. (b) Leakage currents at different voltages. (c) Floating test with 10 h at 1.6 V. (d) Normalized specific capacitances from the long-time floating test.

Fig. 8 shows the voltage holding test, which was performed to evaluate the stability of the LDH/SGN//AC hybrid supercapacitor. As shown in Fig. 8a, the cell voltage of the hybrid supercapacitor dropped gradually with time after the voltage holding test for 3 h. The voltage retention decreased from 89% to 82% with an increase in the holding voltage from 1 to 1.6 V. The corresponding leakage currents (Fig. 8b) are 10.8, 14.4, 16.7, 21.8, 30.5, 62.0 and 92.9 mA g^{-1}, implying the mild decomposition of the electrolyte at high holding voltages. Fig. 8c elucidates the floating test for 10 h at a holding voltage of 1.6 V after charging at a specific current of 2 A g^{-1}. Remarkably, Fig. 8d shows that the specific capacitance of the hybrid supercapacitor was reduced to 110 from 124 F g^{-1} after the floating test for 200 h, demonstrating the excellent stability of the hybrid supercapacitor.

4 Conclusions

In conclusion, hybrid composites with electrostatic interaction were fabricated by virtue of the substitution of negatively charged graphene nanosheets for the interlayer nitrate anions located in an Ni–Co layered double hydroxide during the heterogeneous assembly process. The reinforcement of the

Open Access Article. Published on 31 March 2021. Downloaded on 4/29/2026 6:08:00 AM. This article is licensed under a Creative Commons Attribution-NonCommercial 3.0 Unported Licence.

electrostatic connection between the sulfonated graphene nanosheets and host layers of the Ni–Co layered double hydroxide originated from the enhanced abundance of Ni^{3+} on the surface of the hybrid composite, which was beneficial for reducing the charge transfer resistance, and hence accelerating the electrochemical reactions of the transition metal species at the electrode/electrolyte interface. This unique structure also afforded abundant transport pathways of active protons to promote the diffusion-controlled processes during charge storage reactions. Moreover, the electrostatic interaction between the end members within the hybrid composite resulted in the uniform distribution of LDH nanoclusters on the surface of the sulfonated graphene nanosheets to improve the contact interface between the electrodes and electrolyte, which was advantageous to increase the active sites participating in the charge storage reactions. Remarkably, the LDH/SGN hybrid composite achieved a high specific capacity of 1177 C g^{-1} (2354 F g^{-1}) at a current density of 1 A g^{-1} in addition to retaining a specific capacity of 880 C g^{-1} (1760 F g^{-1}) with an increase in the current density to 10 A g^{-1}, which is beneficial for the fast kinetic processes during the charge storage reactions. Based on the enhancement of the electrostatic interaction within the hybrid composite and the structural stability of the electrode materials, the capacity retention of the LDH/SGN hybrid composite remained 89% after 4000 cycles. A hybrid supercapacitor was assembled using the LDH/SGN hybrid composite as the positive electrode and activated carbon as the negative electrode. When the voltage window of the LDH/SGN//AC hybrid supercapacitor approached 1.6 V, the variation in the specific capacitance from 121 to 80 F g^{-1} followed an increase in the specific current from 1 to 10 A g^{-1}. Besides, the hybrid supercapacitor achieved a maximum energy density of 43 W h kg^{-1} at a power density of 800 W kg^{-1} with a capacitance retention of 94% after 10 000 cycles, suggesting the potential applications of the LDH/SGN hybrid composite as a positive electrode for hybrid supercapacitors.

Conflicts of interest

There are no conflicts to declare.

Acknowledgements

This work was supported by National Natural Science Foundation of China (51702280), Natural Science Foundation of Hebei Province of China (E2020203037), Department of Education of Hebei Province of China (QN2017147).

Notes and references

1 Y. Guo, X. Hong, Y. Wang, Q. Li, J. Meng, R. Dai, X. Liu, L. He and L. Mai, *Adv. Funct. Mater.*, 2019, **29**, 1809004.
2 M. Nawwar, R. Poon, R. Chen, R. P. Sahu, I. K. Puri and I. Zhitomirsky, *Carbon Energy*, 2019, **1**, 124–133.
3 Y. Shi, G. Liu, R. Jin, H. Xu, Q. Wang and S. Gao, *Carbon Energy*, 2019, **1**, 253–275.
4 N. Choudhary, C. Li, J. Moore, N. Nagaiah, L. Zhai, Y. Jung and J. Thomas, *Adv. Mater.*, 2017, **29**, 1605336.
5 Y. Zhao, L. Hu, S. Zhao and L. Wu, *Adv. Funct. Mater.*, 2016, **26**, 4085–4093.
6 H. Kim, M.-Y. Cho, M.-H. Kim, K.-Y. Park, H. Gwon, Y. Lee, K. C. Roh and K. Kang, *Adv. Energy Mater.*, 2013, **3**, 1500–1506.
7 J. Kavil, P. M. Anjana, P. Periyat and R. B. Rakhi, *Sustainable Energy Fuels*, 2018, **2**, 2244–2251.
8 X. Fan, Z. Peng, Y. Yang, H. Zhou and X. Guo, *J. Mater. Chem. A*, 2015, **3**, 10077–10084.
9 J. Yan, Q. Wang, T. Wei and Z. Fan, *Adv. Energy Mater.*, 2014, **4**, 1300816.
10 K. S. Kumar, N. Choudhary, Y. Jung and J. Thomas, *ACS Energy Lett.*, 2018, **3**, 482–495.
11 L. Li, L. Tan, G. Li, Y. Zhang and L. Liu, *Langmuir*, 2017, **33**, 12087–12094.
12 M. K. Paliwal and S. K. Meher, *ACS Appl. Nano Mater.*, 2019, **2**, 5573–5586.
13 S. G. Mohamed, S. Y. Attia, Y. F. Barakat, H. H. Hassan and W. A. Zoubi, *ChemistrySelect*, 2018, **3**, 6061–6072.
14 P. Wen, P. Gong, J. Sun, J. Wang and S. Yang, *J. Mater. Chem. A*, 2015, **3**, 13874–13883.
15 J. Yang, P. Li, L. Wang, X. Guo, J. Guo and S. Liu, *J. Electroanal. Chem.*, 2019, **848**, 113301.
16 S. N. Ansari, M. Saraf, A. K. Gupta and S. M. Mobin, *Chem.–Asian J.*, 2019, **14**, 3566–3571.
17 Y. Wang, W. Zhang, X. Guo, K. Jin, Z. Chen, Y. Liu, L. Yin, L. Li, K. Yin, L. Sun and Y. Zhao, *ACS Appl. Mater. Interfaces*, 2019, **11**, 7946–7953.
18 Y. Gu, L.-Q. Fan, J.-L. Huang, C.-L. Geng, J.-M. Lin, M.-L. Huang, Y.-F. Huang and J.-H. Wu, *J. Power Sources*, 2019, **425**, 60–68.
19 A. Meng, T. Shen, T. Huang, G. Song, Z. Li, S. Tan and J. Zhao, *Sci. China Mater.*, 2020, **63**, 229–239.
20 X. Wang, H. Li, H. Li, S. Lin, J. Bai, J. Dai, C. Liang, X. Zhu, Y. Sun and S. Dou, *J. Mater. Chem. A*, 2019, **7**, 2291–2300.
21 R. Zhao, M. Wang, D. Zhao, H. Li, C. Wang and L. Yin, *ACS Energy Lett.*, 2018, **3**, 132–140.
22 H. Li, F. Musharavati, E. Zalenezhad, X. Chen, K. N. Hui and K. S. Hui, *Electrochim. Acta*, 2018, **261**, 178–187.
23 X. Li, J. Zhou and X. Li, *ChemElectroChem*, 2019, **6**, 4653–4659.
24 N. Joseph, P. M. Shafi and A. C. Bose, *Energy Fuels*, 2020, **34**, 6558–6597.
25 J. Yu, Z. Cui, X. Li, D. Chen, J. Ji, Q. Zhang, J. Sui, L. Yu and L. Dong, *J. Energy Storage*, 2020, **27**, 101165.
26 Y. Jiang, Y. Song, Y. Li, W. Tian, Z. Pan, P. Yang, Y. Li, Q. Gu and L. Hu, *ACS Appl. Mater. Interfaces*, 2017, **9**, 37645–37654.
27 W. Peng, H. Li and S. Song, *ACS Appl. Mater. Interfaces*, 2017, **9**, 5204–5212.
28 J. Xu, S. Gai, F. He, N. Niu, P. Gao, Y. Chen and P. Yang, *Dalton Trans.*, 2014, **43**, 11667–11675.
29 X. Bai, Q. Liu, J. Liu, Z. Gao, H. Zhang, R. Chen, Z. Li, R. Li, P. Liu and J. Wang, *Chem. Eng. J.*, 2017, **328**, 873–883.
30 F. Liu, Y. Chen, Y. Liu, J. Bao, M. Han and Z. Dai, *Nanoscale*, 2019, **11**, 9896–9905.

 © 2021 The Author(s). Published by the Royal Society of Chemistry

Open Access Article. Published on 31 March 2021. Downloaded on 4/29/2026 6:08:00 AM.
This article is licensed under a Creative Commons Attribution-NonCommercial 3.0 Unported Licence.

31 J. Chen, Y. Zhang, M. Zhang, B. Yao, Y. Li, L. Huang, C. Li and G. Shi, *Chem. Sci.*, 2016, **7**, 1874–1881.
32 H. Zhang, C. Peng, J. Yang, M. Lv, R. Liu, D. He, C. Fan and Q. Huang, *ACS Appl. Mater. Interfaces*, 2013, **5**, 1761–1767.
33 J. Qin, Y. Zhang, S. E. Lowe, L. Jiang, H. Y. Ling, G. Shi, P. Liu, S. Zhang, Y. L. Zhong and H. Zhao, *J. Mater. Chem. A*, 2019, **7**, 9646–9655.
34 L. Wang, R. Zhang, Y. Jiang, H. Tian, Y. Tan, K. Zhu, Z. Yu and W. Li, *Nanoscale*, 2019, **11**, 13894–13902.
35 Z. Rahman, X. Xu, U. Katragadda, Y. S. R. Krishnaiah, L. Yu and M. A. Khan, *Mol. Pharmaceutics*, 2014, **11**, 787–799.
36 D. Hanaor, M. Michelazzi, C. Leonelli and C. C. Sorrell, *J. Eur. Ceram. Soc.*, 2012, **32**, 235–244.
37 W. Su, T. Lin, W. Chu, Y. Zhu, J. Li and X. Zhao, *RSC Adv.*, 2016, **6**, 113123–113131.
38 M. Fan, C. Zhu, Z.-Q. Feng, J. Yang, L. Liu and D. Sun, *Nanoscale*, 2014, **6**, 4882–4888.
39 J. Liang and L. Li, *J. Mater. Chem. A*, 2017, **5**, 10998–11008.
40 T. Wang, Y. Xu, Z. He, M. Zhou, W. Yu, B. Shi, C. Song and K. Huang, *React. Funct. Polym.*, 2018, **132**, 98–103.
41 J. Wu and D. Chen, *Prog. Org. Coat.*, 2018, **118**, 116–121.
42 T. Dong, X. Zhang, M. Li, P. Wang and P. Yang, *Inorg. Chem. Front.*, 2018, **5**, 3033–3041.
43 Q. Wu, A. Olafsen, Ø. B. Vistad, J. Roots and P. Norby, *J. Mater. Chem.*, 2005, **15**, 4695–4700.
44 Y. Tan, D. Sun, L. Chen and C. C. Li, *New J. Chem.*, 2016, **40**, 8364–8370.
45 H. Kang, G. Huang, S. Ma, Y. Bai, H. Ma, Y. Li and X. Yang, *J. Phys. Chem. C*, 2009, **113**, 9157–9163.
46 S. Kandula, K. R. Shrestha, G. Rajeshkhanna, N. H. Kim and J. H. Lee, *ACS Appl. Mater. Interfaces*, 2019, **11**, 11555–11567.
47 S. Karthik Kiran, S. Shukla, A. Struck and S. Saxena, *ACS Appl. Mater. Interfaces*, 2019, **11**, 20232–20240.
48 H. Xiong, L. Liu, L. Fang, F. Wu, S. Zhang, H. Luo, C. Tong, B. Hu and M. Zhou, *J. Alloys Compd.*, 2021, **857**, 158275.
49 L. Liu, L. Fang, F. Wu, J. Hu, S. Zhang, H. Luo, B. Hu and M. Zhou, *J. Alloys Compd.*, 2020, **824**, 153929.
50 W. Su, F. Wu, L. Fang, J. Hu, L. Liu, T. Guan, X. Long, H. Luo and M. Zhou, *J. Alloys Compd.*, 2019, **799**, 15–25.
51 T. Guan, L. Fang, L. Liu, F. Wu, Y. Lu, H. Luo, J. Hu, B. Hu and M. Zhou, *J. Alloys Compd.*, 2019, **799**, 521–528.
52 Z. Wang, H. Su, F. Liu, X. Chu, C. Yan, B. Gu, H. Huang, T. Yang, N. Chen, Y. Han, W. Deng, H. Zhang and W. Yang, *Electrochim. Acta*, 2019, **307**, 302–309.
53 J. Zhi, S. Deng, Y. Zhang, Y. Wang and A. Hu, *J. Mater. Chem. A*, 2013, **1**, 3171–3176.
54 Y. Ouyang, O. Geuli, Q. Hao and D. Mandler, *ACS Appl. Energy Mater.*, 2020, **3**, 1784–1793.
55 N. L. Wulan Septiani, Y. V. Kaneti, K. B. Fathoni, J. Wang, Y. Ide, B. Yuliarto, A. Nugraha, H. K. Dipojono, A. K. Nanjundan, D. Golberg, Y. Bando and Y. Yamauchi, *Nano Energy*, 2020, **67**, 104270.
56 Y. Liu, Y. Wang, C. Shi, Y. Chen, D. Li, Z. He, C. Wang, L. Guo and J. Ma, *Carbon*, 2020, **165**, 129–138.
57 H. Liang, J. Lin, H. Jia, S. Chen, J. Qi, J. Cao, T. Lin, W. Fei and J. Feng, *J. Power Sources*, 2018, **378**, 248–254.
58 S. Giri, D. Ghosh and C. K. Das, *Adv. Funct. Mater.*, 2014, **24**, 1312–1324.
59 H. Qiu, X. Sun, S. An, D. Lan, J. Cui, Y. Zhang and W. He, *Dalton Trans.*, 2020, **49**, 6391–6397.
60 X. Bai, Q. Liu, Z. Lu, J. Liu, R. Chen, R. Li, D. Song, X. Jing, P. Liu and J. Wang, *ACS Sustainable Chem. Eng.*, 2017, **5**, 9923–9934.
61 J. Cao, L. Li, Y. Xi, J. Li, X. Pan, D. Chen and W. Han, *Sustainable Energy Fuels*, 2018, **2**, 1350–1355.
62 K. Sekar, G. Raji, S. Chen, S. Liu and R. Xing, *Appl. Surf. Sci.*, 2020, **527**, 146856.